



# Metal–silicate partitioning of tungsten at high pressure and temperature: Implications for equilibrium core formation in Earth

Elizabeth Cottrell<sup>a,\*</sup>, Michael J. Walter<sup>b</sup>, David Walker<sup>c</sup>

<sup>a</sup> Department of Mineral Sciences, National Museum of Natural History, Smithsonian Institution, 10th & Constitution Ave., Washington DC, 20560, USA

<sup>b</sup> Department of Earth Sciences, University of Bristol, Queen's Road, Bristol BS8 1RJ, United Kingdom

<sup>c</sup> Lamont-Doherty Earth Observatory, Department of Earth and Environmental Sciences, Columbia University, Rt 9W, Palisades, NY 10964, USA

## ARTICLE INFO

### Article history:

Received 20 May 2008

Received in revised form 6 February 2009

Accepted 26 February 2009

Available online 1 April 2009

Editor: A.W. Hofmann

### Keywords:

core formation

partitioning

siderophile

tungsten

w

experiments

carbon

## ABSTRACT

Tungsten partitioning between liquid metal and liquid silicate,  $D(W)$ , from 1723–2673 K, 0.5–18 GPa, and over a wide range of metal and silicate compositions provides constraints on planetary core formation models. We find that W partitioning is extremely sensitive to the carbon content of the metal alloy, becoming about an order of magnitude more siderophile at carbon saturation. Activity-composition corrections based on interactions between W–C and Fe–C in metal solution shift calculated  $D(W)$  to more lithophile values, and calculated oxygen fugacities ( $fO_2$ ) to more oxidizing values, than uncorrected data. W exists as a highly charged cation in silicate solution, displaying a mixture of oxidation states from +4 to +6 in experiments at  $fO_2$  of  $\sim 0.5$ –2 log units below the iron–wüstite buffer. At constant  $fO_2$ , the average calculated valence decreases with pressure from  $\sim +5.5$  at 0.5 GPa to  $\sim +4$  at 11–18 GPa. As a result of its high oxidation state, W partitioning is strongly dependent on silicate melt polymerization and  $fO_2$ . In contrast to some previous results, we find that  $D(W)$  may decrease slightly in response to increasing temperature in the pressure range of our experiments. Pressure exerts a non-monotonic effect:  $D(W)$  increases with pressure up to  $\sim 3$  to 4 GPa, but decreases at higher pressures. Previous models for the effects of pressure and temperature on W partitioning that conflict with our results appear to result from a conflation of the intensive parameters of pressure, temperature, and carbon content.

The mantle abundance of W could have been set by single-stage metal–silicate equilibration along the liquidus in a deep peridotite magma ocean at pressures from 20–50 GPa, and at oxygen fugacities consistent with the mantle's present iron budget ( $IW = 2$  to  $-2.5$ ). Equilibration at higher pressure is viable if the core-forming metal contained a significant, but not unreasonable, abundance of carbon ( $\sim 2$  wt.%). Recent continuous accretion models involving multi-stage metal–silicate equilibration in a deepening magma ocean with progressive oxidation of the silicate remain permissible given our new treatment of W partitioning data.

Published by Elsevier B.V.

## 1. Introduction

Planetary accretion is sufficiently energetic to segregate undifferentiated material into metallic cores and silicate mantles and may lead to widespread melting at the planetesimal scale early in the history of the solar system (Ghosh and McSween, 1998; Yin et al., 2002; Yoshino et al., 2003). Gravitational potential energy release and large late-stage impacts among planetary embryos can also cause large-scale melting that may have led to one or more deep magma oceans on Earth (Davies, 1985; Sasaki and Nakazawa, 1986; Benz and Cameron, 1990; Tonks and Melosh, 1993; Canup and Righter, 2000; Chambers, 2004). During this impact–accretion epoch ( $\sim 100$  m.y.), segregation of Earth's core likely involved metal–silicate equilibration at high pressure and temperature in a magma ocean.

The siderophile elements have a chemical affinity for iron metal, and so disproportionately partitioned into metal during core formation, leaving the primitive mantle depleted in those elements. The siderophile element abundance in the modern mantle may provide a record of the physical conditions of core formation, such as the average temperature, pressure, and silicate and metal compositions, if metal and silicate were ever in equilibrium during segregation. For this reason, considerable effort has gone into the investigation of equilibrium partitioning of the siderophile elements between metal and silicate.

Experimental partitioning results for Ni and Co have provided the most robust geochemical evidence for high-pressure equilibration between metal and silicate (Thibault and Walter, 1995; Li and Agee, 1996, 2001; Chabot et al., 2005). Multi-element models involving these and other moderately siderophile elements (e.g. W, Mo, P) are also permissive of high pressure–temperature equilibration (Righter et al., 1997; Righter and Drake, 1999). Overall, moderately siderophile element constraints have led to

\* Corresponding author. Tel.: +1 202 633 1859.

E-mail address: [CottrellE@si.edu](mailto:CottrellE@si.edu) (E. Cottrell).

**Table 1**  
Experimental conditions and results.

Run#	SC	Capsule	Time (s)	P (GPa)	T (K)	log $f_{O_2}^{1,2}$	log $f_{O_2}$ corrected for Fe–C interaction	nbo/t <sup>3</sup>	logD (molar)	logD (molar) corrected, W–Fe(±C) interaction
W05.1a	C	C	300	0.5	2100	–1.54 (1)	–1.22	2.59	2.08 (1)	1.70
W05.1b	D2	C	300	0.5	2100	–1.64 (2)	–1.35	2.30	2.76 (45)	2.35
W05.2a	A2	C	300	0.5	2100	–1.89 (1)	–1.60	2.29	3.03 (14)	2.64
W05.2b	I	C	300	0.5	2100	–1.60 (1)	–1.31	2.66	2.23 (2)	1.84
W05.3	A3	C	300	0.5	2100	–2.18 (1)	–1.88	3.28	2.15 (6)	1.76
W1.04	A	C	900	1	2100	–1.84 (1)	–1.55	2.14	3.04 (7)	2.67
W1.05	B2	C	900	1	2100	–1.59 (2)	–1.31	3.46	1.58 (3)	1.20
W1.06	D2	C	900	1	2100	–1.77 (1)	–1.47	2.94	2.24 (2)	1.86
W1.07	H	C	900	1	2100	–1.36 (1)	–1.06	2.51	2.12 (3)	1.73
W1.08	D2	C	900	1	2100	–1.68 (1)	–1.37	2.26	2.69 (4)	2.31
W1.09	A2	C	900	1	2100	–2.07 (1)	–1.79	3.03	2.42 (4)	2.04
W1.10	B2	C	900	1	2100	–1.36 (2)	–1.06	2.65	1.85 (5)	1.48
W1.11	G	C	900	1	2100	–1.44 (1)	–1.14	2.36	2.25 (6)	1.87
W1.12	C3	C	900	1	2100	–1.92 (3)	–1.64	1.27	3.55 (23)	3.14
W1.13	A3	C	900	1	2100	–2.17 (1)	–1.86	2.14	3.35 (10)	2.97
W1.14	C	C	900	1	2100	–1.59 (1)	–1.31	2.66	2.05 (3)	1.68
W1.15	C2	C	900	1	2100	–1.80 (1)	–1.55	3.36	1.83 (2)	1.48
W08	C	C	600	2	2300	–1.59 (1)	–1.26	2.73	2.35 (5)	1.84
W10	A	C	600	2	2300	–2.06 (1)	–1.69	2.06	3.64 (10)	3.13
W12	B	C	600	2	2300	–1.35 (4)	–1.00	2.74	1.89 (7)	1.36
W17	D	C	600	2	2300	–1.74 (1)	–1.38	2.19	3.14 (4)	2.65
W20	E	C	600	2	2300	–1.42 (1)	–1.08	2.83	2.07 (3)	1.55
W34	F	C	600	2	2300	–1.65 (1)	–1.30	2.26	2.92 (6)	2.42
W39	G	C	600	2	2300	–1.39 (1)	–1.07	2.36	2.56 (1)	2.07
W43	H	C	600	2	2300	–1.29 (1)	–0.95	2.50	2.29 (2)	1.79
PC579	H	C	10800	2	2200	–1.09 (1)	–0.88	2.29	2.25 (4)	1.86
W47	A2	C	600	2	2300	–1.90 (1)	–1.55	2.30	3.18 (6)	2.68
W54	C2	C	600	2	2300	–1.80 (1)	–1.46	3.54	1.93 (5)	1.43
W55	B2	C	600	2	2300	–1.59 (4)	–1.25	3.62	1.70 (6)	1.18
W56	D2	C	600	2	2300	–1.90 (1)	–1.54	3.00	2.54 (6)	2.03
W57	I	C	600	2	2300	–1.40 (1)	–1.03	2.58	2.37 (3)	1.91
W58	A3	C	600	2	2300	–2.06 (3)	–1.73	3.09	2.66 (5)	2.16
W59	C3	C	600	2	2300	–1.82 (1)	–1.49	1.35	3.71 (6)	3.17
W63	A	MgO	600	2	2300	–2.65 (3)	–	4.07	2.24 (2)	2.78
W73	B	C	600	2	2450	–1.20 (3)	–0.87	2.80	1.78 (3)	1.10
W74	C2	C	600	2	2450	–1.52 (3)	–1.16	3.36	1.64 (4)	1.05
W75	H	C	600	2	2450	–1.38 (1)	–1.00	2.25	2.48 (3)	1.89
W76	A3	C	600	2	2450	–2.26 (3)	–1.87	2.90	2.79 (5)	2.20
W77	D2	C	600	2	2450	–1.87 (1)	–1.51	2.77	2.53 (6)	1.97
W78	C	C	600	2	2450	–1.51 (2)	–1.16	2.55	2.24 (5)	1.63
W83	B2	C	600	2	2450	–1.54 (2)	–1.17	3.38	1.69 (3)	1.07
W84	C3	C	600	2	2450	–1.83 (1)	–1.47	1.25	3.76 (12)	3.14
W15	C	C	360	2	2600	–1.64 (2)	–1.18	2.65	2.37 (4)	1.64
W16	B	C	500	2	2600	–1.39 (4)	–0.93	2.79	1.96 (5)	1.24
W18	D	C	500	2	2600	–1.72 (1)	–1.27	2.20	3.06 (6)	2.33
W22	E	C	500	2	2600	–1.47 (2)	–1.01	2.79	2.06 (4)	1.34
W23	A	C	500	2	2600	–2.01 (1)	–1.55	2.10	3.49 (4)	2.80
W24	D	C	600	2	2600	–1.77 (1)	–1.30	2.18	3.08 (6)	2.38
W37	F	C	500	2	2600	–1.66 (1)	–1.19	2.18	2.94 (4)	2.24
W40	G	C	500	2	2600	–1.48 (1)	–1.01	2.39	2.57 (2)	1.87
W44	H	C	500	2	2600	–1.32 (1)	–0.85	2.50	2.33 (2)	1.63
W48	A2	C	500	2	2600	–1.90 (1)	–1.44	2.25	3.13 (4)	2.41
W79	B	C	500	2	2600	–1.29 (5)	–0.88	2.62	1.96 (4)	1.20
W80	C2	C	500	2	2600	–1.76 (1)	–1.30	3.48	1.99 (4)	1.27
W85	B2	C	500	2	2600	–1.48 (2)	–1.04	3.40	1.62 (4)	0.87
W86	C3	C	500	2	2600	–1.87 (1)	–1.44	1.24	3.86 (11)	3.13
4P102303	MAR	W	28800	2.1	1873	–1.00 (1)	–	0.78	2.97 (1)	3.72
4P080905	B + Qz	W	68400	2.3	1873	–1.23 (2)	–	0.51	3.2 (2)	3.96
GG082305	B + Qz	W	14400	2.2	2073	–0.56 (1)	–	0.52	2.6 (1)	3.24
GG080405	B + Qz	W	12600	2.3	2300	–1.51 (10)	–	0.53	3.61 (10)	4.15
GG081005	B + Qz	W	7200	2.3	2673	–1.80 (28)	–	0.52	3.95 (28)	4.35
GG091603	MAR	W	30600	2.0	1723	–1.12 (40)	–	0.78	3.02 (40)	3.89
3P121405	MAR	W	36600	2.2	1873	–1.41 (1)	–	0.88	3.13 (10)	3.89
GL112105	MAR	W	14400	2	2073	–1.77 (1)	–	0.90	3.09 (6)	3.73
GG092103	MAR	W	14400	2.1	2073	–0.67 (1)	–	0.75	2.7 (1)	3.35
GG082705	MAR	W	32400	2.1	2073	–1.86 (1)	–	0.87	3.89 (36)	4.53
GG091103	MAR	W	3600	2.1	2273	–0.67 (1)	–	0.77	2.76 (3)	3.31
3P121605	MAR	W	5700	2.2	2273	–1.30 (1)	–	0.90	3.36 (3)	3.91
GG102403	MAR	W	3600	2.2	2473	–0.83 (6)	–	0.77	2.95 (6)	3.42
3P121705	MAR	W	3720	2.2	2473	–1.00 (1)	–	0.87	3.1 (11)	3.57
GG121705	MAR	W	3300	2.3	2673	–1.55 (1)	–	0.85	2.89 (19)	3.29
GG102103	MAR	W	3600	2.1	2673	–0.80 (1)	–	0.74	2.95 (3)	3.35
pc572	KLB-1	W	10800	2.2	2173	–2.08 (1)	–	2.78	2.62 (1)	3.21
pc580	I	W	1800	2	2300	–1.35 (1)	–	2.33	2.33 (3)	2.87

Table 1 (continued)

Run#	SC	Capsule	Time (s)	P (GPa)	T (K)	log $f_{O_2}^{1,2}$	log $f_{O_2}$ corrected for Fe–C interaction	nbo/t <sup>3</sup>	logD (molar)	logD (molar) corrected, W–Fe(±C) interaction
W01	A	C	300	6	2300	–2.20 (2)	–1.87	2.13	3.48 (6)	3.02
W09	C	C	300	6	2300	–1.73 (2)	–1.42	2.81	2.43 (6)	1.94
W19	E	C	300	6	2300	–1.45 (1)	–1.12	2.76	2.21 (3)	1.68
W28	D	C	300	6	2300	–1.86 (2)	–1.54	2.24	3.23 (8)	2.72
W29	E	C	360	6	2300	–1.45 (2)	–1.11	2.81	2.16 (3)	1.66
W32	C	C	360	6	2300	–1.65 (2)	–1.32	2.81	2.41 (8)	1.89
W33	B	C	360	6	2300	–1.35 (3)	–1.02	2.83	2.05 (5)	1.51
W38	F	C	360	6	2300	–1.61 (1)	–1.27	2.32	2.87 (4)	2.39
W41	G	C	360	6	2300	–1.41 (1)	–1.09	2.41	2.46 (3)	1.98
W42	H	C	500	6	2300	–1.31 (1)	–0.96	2.46	2.39 (2)	1.91
W49	A2	C	360	6	2300	–1.88 (1)	–1.55	2.32	3.13 (6)	2.65
W91	C2	C	360	6	2300	–1.57 (1)	–1.29	3.48	1.71 (1)	1.25
W45	D	C	360	6	2700	–1.96 (2)	–1.45	2.68	2.79 (4)	2.02
W46	G	C	360	6	2700	–1.51 (2)	–0.99	2.58	2.46 (3)	1.71
W50	A2	C	360	6	2700	–1.91 (2)	–1.41	2.29	2.99 (4)	2.21
W51	A	C	360	6	2700	–2.00 (1)	–1.50	2.21	3.15 (5)	2.37
W81	C2	C	360	6	2700	–1.57 (2)	–1.13	3.34	1.96 (5)	1.20
W92	B	C	150	6	2700	–1.22 (9)	–0.90	3.03	1.76 (11)	0.82
W62	A	C	300	11	2400	–1.75 (15)	–1.42	2.44	2.32 (13)	1.75
W68	A3	C	300	11	2400	–1.72 (11)	–1.37	3.28	1.66 (14)	1.15
W87	G	C	120	11	2400	–1.39 (5)	–1.09	3.06	1.65 (11)	1.02
W90	D	C	120	11	2400	–1.48 (4)	–1.16	2.17	2.30 (7)	1.80
W64	D	C	300	18	2500	–1.42 (3)	–1.07	2.01	2.37 (6)	1.71
W65	A	C	300	18	2500	–1.75 (3)	–1.39	2.23	2.46 (5)	1.87
W88	A3	C	30	18	2500	–1.44 (2)	–1.12	3.20	1.60 (4)	0.98
W89	G	C	120	18	2500	–1.40 (3)	–1.05	2.17	2.07 (5)	1.47
W94	B	C	300	18	2500	–1.17 (3)	–0.85	2.61	1.44 (3)	0.84
W95	D2	C	300	18	2500	–1.80 (4)	–1.50	2.73	2.01 (8)	1.52

\*Experiments previously reported by [Walter and Thibault \(1995\)](#), but reanalyzed here (note: *D* is also calculated on a mole basis in the present study).

<sup>1</sup>Errors in parentheses reflect microprobe precision only and are equal to two standard errors propagated in quadrature.

<sup>2</sup>Many of the carbon-free experiments are solubility experiments in solid W metal capsules with insufficient iron to form a liquid Fe–alloy phase. In these experiments the oxygen fugacity may be estimated using the tungsten–tungsten oxide buffer (WWO2) in analogy to iron–wüstite, and then related to  $\Delta IW$  using the known offset between  $IW$  and WWO2 at 1 atm from [O'Neill and Pownceby \(1993\)](#). This estimation of  $f_{O_2}$  has a large associated uncertainty; however, in experiments with measurable Fe in the solid or liquid metal, comparison of the  $f_{O_2}$  calculated using Eq. (2) to that calculated using the WWO2 buffer yields estimates that agree to within 0.5 log units. The C-free experiments ranged in oxygen fugacity from approximately  $IW-2$  to  $-0.5$ .

<sup>3</sup>W's effect on melt polymerization was ignored because it is unknown whether it acts as a network former or modifier and inclusion of W in either capacity has very little effect on the calculated value of nbo/t for these experiments where W is typically <0.5 wt.%. Parameterization by optical basicity ([Mills, 1993](#)) and nbo/t are indistinguishable.

'single-stage' core segregation models with equilibration at pressures generally in the range of 30–50 GPa. Recently, the inclusion of additional slightly siderophile elements (e.g. V, Nb, Si) has led to more complex multi-stage models of core formation in which conditions become progressively more oxidizing ([Wade and Wood, 2005](#); [Wood et al., 2008](#)).

After Ni and Co, W is the most intensively studied element experimentally, and provides compositional constraints that Ni and Co do not ([Walter and Thibault, 1995](#)). Tungsten is highly refractory and requires no volatility correction and is also only moderately siderophile so that its mantle abundance is not easily displaced by the late addition of meteoritic material. A compilation of W metal/silicate partitioning data published prior to 2008 (11 studies consisting of 114 experiments) reveals a spread of over 3 orders of magnitude in partition coefficients, even when effects of oxygen fugacity and melt composition are considered. Moreover, regression of the compiled data in *T*, *P*,  $f_{O_2}$ , or composition space across these studies yields dependencies that are in conflict with those reported within individual data sets in isolation. In this study we constrain the partitioning behavior of W as a function of *P*, *T*,  $f_{O_2}$ , silicate melt composition, and metal carbon content. We use the results to ascertain whether or not W partitioning is compatible with various models for core formation in Earth.

## 2. Methods

### 2.1. Strategy

We report results from 103 experiments to determine the partition coefficient (*D*) of W between liquid metal and liquid silicate; thirty of the experiments were presented previously by [Walter and Thibault](#)

(1995). We define the partition coefficient, *D*, as the molar activity of W in the metal divided by the molar activity of W in the silicate melt.

$$D = \frac{a_W^{\text{metal}}}{a_W^{\text{silicate}}} \quad (1)$$

We apply this definition throughout the remainder of this contribution, unless otherwise noted, recalculating the results of other studies for comparison. We approximate  $a_W^{\text{silicate}}$  as the W atomic fraction because  $WO_3$  activity coefficients have only been reliably determined in highly polymerized melts ([O'Neill et al., 2008](#)) relative to those studied here, and because hexavalent W is not the dominant species in all of our experiments (discussed below). We investigated the effects of temperature (*T*), pressure (*P*), melt composition, oxygen fugacity ( $f_{O_2}$ ), and carbon content ( $X_C$ ) on *D*, with W as the principal solute in the system (other than carbon). We varied the compositional parameters in sets of isobaric, isothermal experiments.

### 2.2. Starting compositions

A wide range of natural and synthetic starting compositions was employed ([Supplemental Table A](#)). Thirteen synthetic compositions (A–I) were prepared in the system Si–Al–Fe–Mg–Ca–O. Mixtures of model basalt, komatiite, peridotite, and CI chondrite were prepared from high purity oxides (CaO added as  $CaCO_3$  which was then decarbonated). Iron was added to these “mother mixtures” as finely powdered Fe-metal and  $Fe_2O_3$  to create “daughter mixtures” with variable total oxygen content. Approximately 10 wt.% finely powdered pure W metal was added to daughter mixtures to ensure detection in the silicate with electron microprobe, except one to which only 5% was added. The

experimental metals contain significantly more W, typically about 30 wt.%, than the level expected in Earth's core (~500 ppm). However, Walter and Thibault (1995) performed experiments using 5 and 10 wt.% W in the bulk and found no difference in W partitioning, indicating an inconsequential compositional dependence in this range. Ertel et al. (1996) determined that the limits of Henry's Law behavior for W dissolved in the silicate occur at 6.5 wt.% W at 1400 °C, and 14 wt.% at 1500 °C, whereas the highest W concentrations in the silicates reported here are <3 wt.%, and most experiments contain less than 1 wt.%.

In addition, experiments were also performed on three natural compositions: a basalt powder from the Mid-Atlantic Ridge (All-129-6), that same basalt plus 25% quartz by weight, and Kilbourne Hole peridotite powder KLB-1. Pure W or Fe–W capsules served as the W source in the natural composition experiments. The 15 starting compositions, from model andesite to peridotite, allowed us to investigate the effects of silicate melt composition on partitioning (Supplemental Table A).

### 2.3. Experiments

Piston-cylinder experiments were performed at nominal pressures of 0.5, 1, and 2 GPa and from 1723–2673 K using 1/2 in. Boyd–England style devices. Two distinct capsule-assembly combinations were used: (1) Standard talc-pyrex assemblies with graphite capsules (Thibault and Walter, 1995) and (2) the high-temperature assembly of Cottrell and Walker (2006) using tungsten capsules  $\pm$  Fe metal powder. Experiments at 6, 11 and 18 GPa were made in multi-anvil apparatus with samples contained within graphite capsules. Graphite capsule experiments on synthetic compositions were held at temperature for 300 to 900 s whereas those employing W  $\pm$  Fe capsules were held for 1–10 h (Walter et al. (1995), Table 1 and Supplemental Methods). Time-series on similar systems have shown that this is sufficient to obtain a steady-state molten-metal/liquid-silicate partition coefficient at these temperatures (Thibault and Walter, 1995); however, we describe additional times series tests below.

### 2.4. Analytical methods

All experiments were embedded in epoxy, then ground and polished to expose the experimental products in cross section. Experiments were examined optically and with scanning electron microscopy with a backscatter detector (Fig. 1). Samples quenched to a segregation of metal alloy plus silicate (either glass or quench-crystallized, Fig. 1). Samples were analyzed by electron microprobe. Nearly all the quenched silicates contained between 0.1 and 3.0 wt.% W, well above the empirically established practical detection limit of 0.02 wt.% W, although a few experiments had less than 0.05%. The compositions of silicate and metal phases in all experiments and details of the analytical procedures, including assessment of metal carbon contents, are given in Supplemental Data Table B and Supplemental Methods.

## 3. Results

### 3.1. Phase relations and compositions of the run products

A potential difficulty in melting experiments is the interaction of the capsule material with the melt it contains. Of the highly refractory capsule materials, oxide capsules (MgO, Al<sub>2</sub>O<sub>3</sub>) react progressively with the silicate melt, making this an unattractive choice for W because silicate melt composition strongly influences W partitioning. In contrast, graphite capsules are relatively inert with respect to the silicate melt, but react with the metal phase. In the simple system W + graphite + silicate melt (i.e. iron absent), the undesirable equilibrium assemblage is glass plus stable,

stoichiometric solid tungsten-carbide (WC). The reaction of W and C to form carbide is time and temperature dependent (Cottrell, 2004, available upon request). We circumnavigated carbide-formation in the present study by (1) adding sufficient Fe metal to the system to generate liquid Fe alloy and correcting for W–C and Fe–C interactions in the alloy. In this manner we retain the desirable properties of a graphite capsule and are still able to quantify W partitioning between liquid iron alloy and silicate melt. Or (2) forgoing graphite and using W capsules. These experiments were carbon-free.

In the series of graphite capsule experiments with synthetic compositions A–I, the silicate was totally molten and coexisted with molten iron alloy. The liquid Fe-alloy was found upon quench to be cleanly separated from the silicate melt as metal spheres with a variety of textures. Some metals quenched to homogeneous, very fine quench crystallites (Fig. 1a). Others had several forms of dendritic intergrowths including graphite laths and Fe–W–C carbide feathers and rosettes (Fig. 1b). In some experiments liquid metal contained euhedral Fe–W–C carbide crystals that we consider to be liquidus phases (Fig. 1c). The liquid metal in the carbon-bearing experiments ranged near compositions  $\sim$ Fe<sub>60–68</sub>:W<sub>30–40</sub>:C<sub>3–7</sub> by weight.

Metal phase equilibria in our carbon-bearing experiments can be understood in terms of the ternary system Fe–W–C. In Fig. 2b we plot the metal compositions from relevant experiments on the Fe-rich portion of the Fe–W–Gr phase diagram along with phase boundaries from the metallurgical literature (Uhrenius, 1980; Gustafson, 1987). The carbon content of liquid Fe–W alloy coexisting with graphite increases with increasing temperature. When the W content of the alloy becomes sufficiently high, carbide becomes a stable phase coexisting with carbon-saturated liquid Fe–W alloy and graphite, consistent with our observations (Fig. 1c). Because the three phase divariant points track to higher W and C contents in the liquid as temperature rises, it is highly likely that dendritic carbide precipitated out of the metal as temperature fell upon quench. For example, consider a carbide-free liquid in equilibrium with graphite at 1773 K, the point marked by a star in Fig. 2b. Upon cooling, that composition will shift to the three phase field carbide + liquid + graphite.

Experiments on synthetic compositions in graphite capsules from Table 1 (all  $\geq$  2100 K) equilibrated for 30–900 s. The reaction of W with C in liquid metal to form WC complexes in liquid metal or solid WC crystals depends on both time and temperature. Time series show that the shorter duration graphite capsule experiments are equilibrium experiments and are not in the process of converting W to solid carbide. Experiment PC579 (3 h duration) mirrored experiment W43 (600 s). Only small (<10  $\mu$ m) euhedral crystals of carbide were observed in both PC579 and W43 within large pools of iron metal. The partition coefficients of PC579 and W43 agree within two standard errors, implying that the high-temperature graphite capsule experiments equilibrate within minutes.

In the series of tungsten capsule experiments, the samples quenched to silicate + solid W metal (Fig. 1d), or quench silicate + liquid Fe–W alloy (40–70 wt.% W) + solid W metal (Fig. 1e–f). We will refer to these experiments, plus experiment W63 which used an MgO capsule, as carbon-free. The solid and liquid metal compositions were in excellent agreement with those expected for the Fe–W binary (Fig. 2a and Supplemental Data Table B).

### 3.2. The influence of carbon on W partitioning

Carbon saturation in liquid iron-alloy increases the W partition coefficient (D) by about one order of magnitude. The considerable influence of carbon in the metal–silicate system is unsurprising when one considers documented strong interaction between W and C in solid metal/liquid metal systems (Uhrenius, 1980; Gustafson, 1987; Chabot et al., 2006) and in prior studies of metal–silicate partitioning (e.g. Jana and Walker, 1997a; Righter and Drake, 1999).

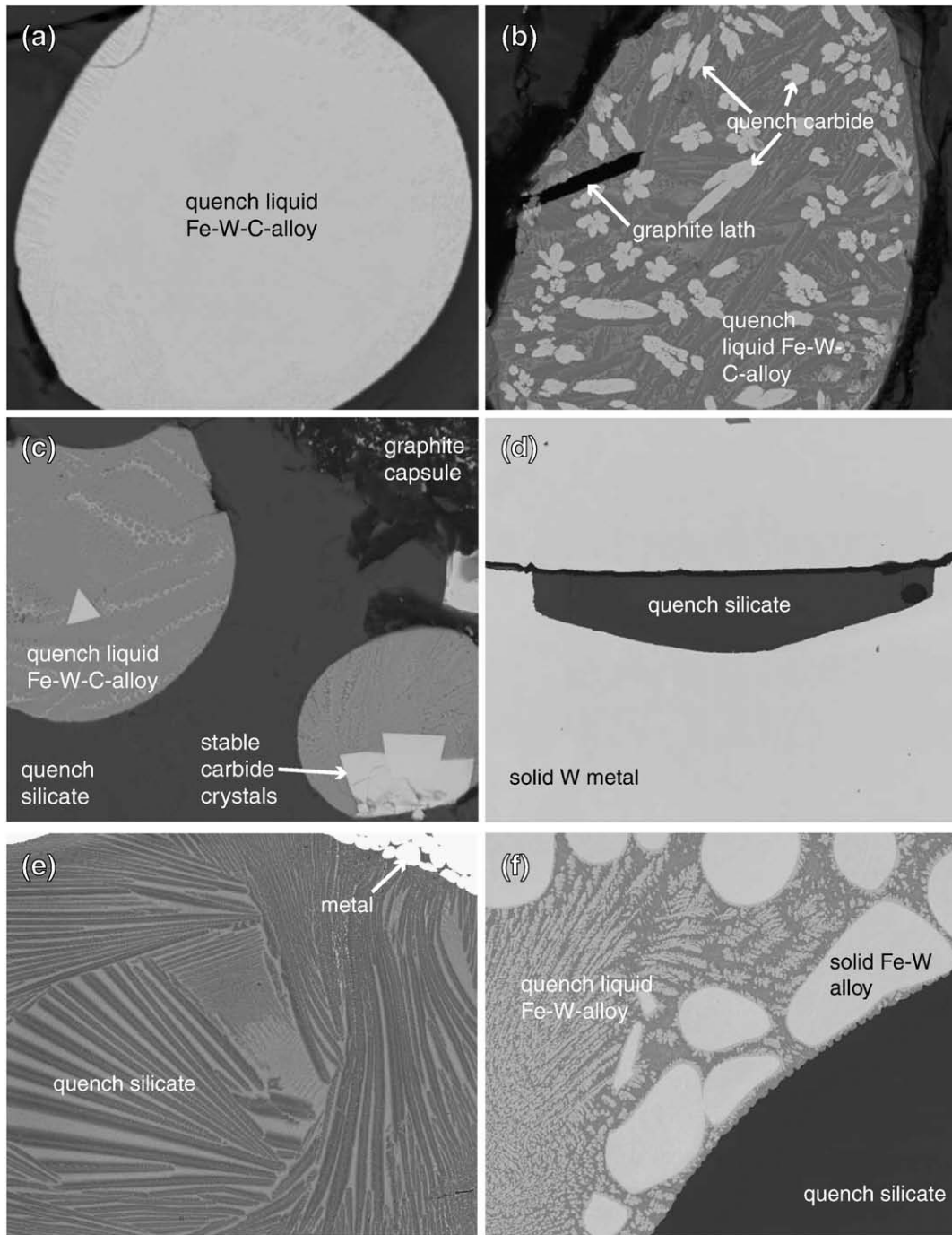


**Fig. 1.** Backscatter electron images of experimental run products consisting of quenched Fe alloy and silicate glass. The darkest gray areas in each frame are quenched silicate glass, with the exception of figures b and c in which graphite is present and annotated. Brighter areas are metal alloys and carbide as described for each figure. (a) Experiment W1.04: quenched liquid Fe–W–C–alloy metal in equilibrium with silicate glass (darkest gray at edges). The metal is saturated with C, but no carbide is present. Field of view is 45  $\mu\text{m}$ . (b) Experiment W73: quenched liquid Fe–W–C–alloy metal in equilibrium with silicate (darkest gray at edges). The quenched liquid consists of dendritic quench laths of W-rich and W-poor Fe-alloy (light and medium grays), and what we interpret as quench crystals of carbide (brightest white). Also present is a single graphite lath of unknown stability at *P* and *T*. Field of view is 120  $\mu\text{m}$ . (c) Experiment W1.10: quenched alloy and glass with large stable crystals of carbide present in each of the pools of quenched liquid Fe–W–C alloy. The graphite capsule is visible in the upper right corner. Field of view is 110  $\mu\text{m}$ . (d) Experiment GG091103: A solid W capsule experiment (C-free) containing a pool of quenched basaltic silicate glass. A decompression crack is visible along the upper edge of the silicate. Field of view is 1.8 mm. (e) Quenched peridotitic silicate melt in experiment PC580: A W capsule experiment (C-free) with added Fe metal. A range of fine to coarse quench textures are visible in the silicate. Field of view is 800  $\mu\text{m}$ . (f) Experiment PC572: A W capsule experiment (C-free) with added Fe metal + KLB-1 peridotite. A large pool of silicate glass adjacent to quenched liquid W–Fe alloy with dendritic texture. Large “blobs” of solid W–Fe alloy float in the quenched liquid alloy; W-rich liquid metal dendrites nucleate on quench at the edge of solid W. Field of view is 250  $\mu\text{m}$ .

### 3.3. Activity corrections

As noted above, the partition coefficients reported in this study are calculated on an atomic basis (with oxygen as O). To account for solute–solute interactions in the iron alloy we employed the algorithm

of Wade and Wood (2005), coded as program METAL, for calculation of solute activities in solvent liquid iron. METAL is based on a modified Wagner formalism that utilizes tabulated interaction parameters and temperature extrapolations presented in the *Steelmaking Data Sourcebook* (1988) and the thermodynamic approach of Ma (2001).

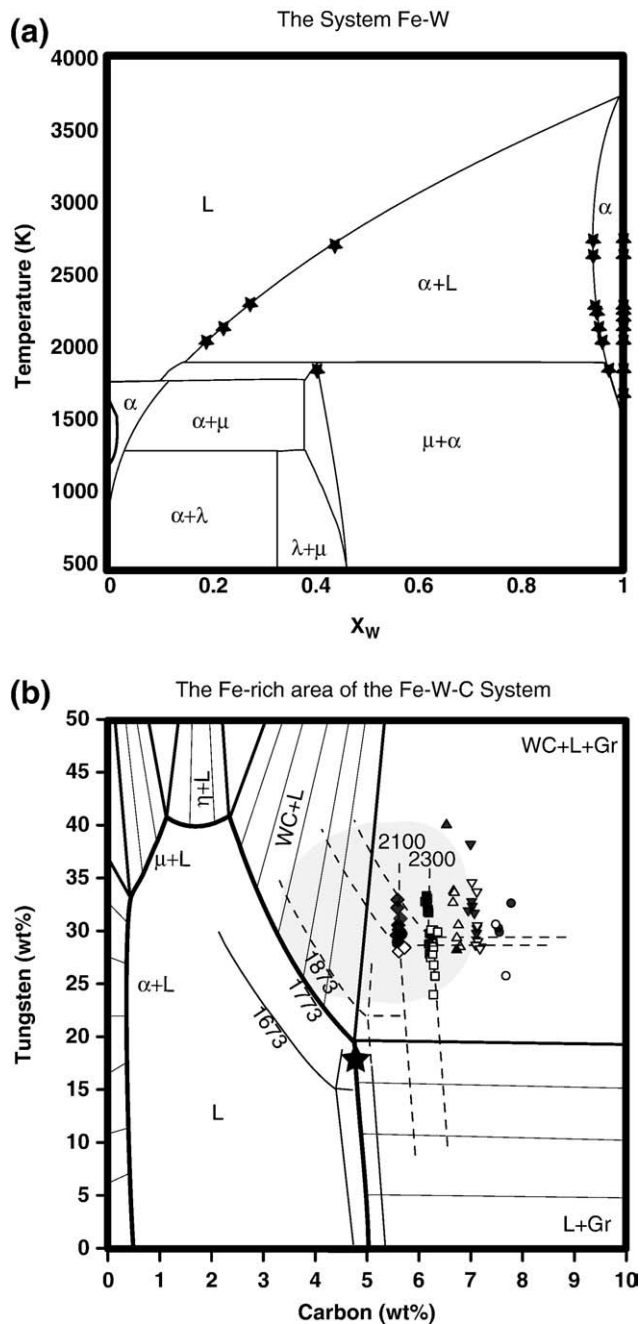


**Fig. 2.** Phase diagrams for the experimental systems. (a) Experiments in the binary system Fe–W at 1 atm, after Gustafson (1987). Stars mark the measured experimental compositions and temperatures for W capsule experiments. Measured liquid and solid compositions at 2.3 GPa show no deviation from the 1 atm values. (b) Phase relations in the Fe-rich portion of the ternary system C–W–Fe at 1773 K, after Uhrenius (1980). Solid isotherms are shown for the known positions of the three-phase equilibria involving liquid-carbide-graphite as a function of temperature from Uhrenius (1980). Dashed lines are the equilibrium saturation surfaces we mapped at high temperatures. The measured experimental compositions (carbon “by difference”) are shown by the light gray shaded field. Experimental compositions corrected by METAL are shown by symbols. Open symbols are completely carbide-free quenched liquid metals; shaded symbols are carbide-bearing metals, with either quench-nucleated or stable carbide crystals (see Fig. 1). Diamonds = 2100 K, squares = 2300 K, “up” triangles = 2450 K, “down” triangles = 2500 K, circles = 2600 K. The large star demonstrates a possible equilibrium composition at 1773 K between liquid alloy and graphite which, upon thermal quench, could move to the three phase field and nucleate carbide due to the drop in temperature.

The program inputs are the experimentally determined elemental mole fractions and the run temperature, and the program outputs are the liquid iron and solute activities (Wade and Wood, 2005). In

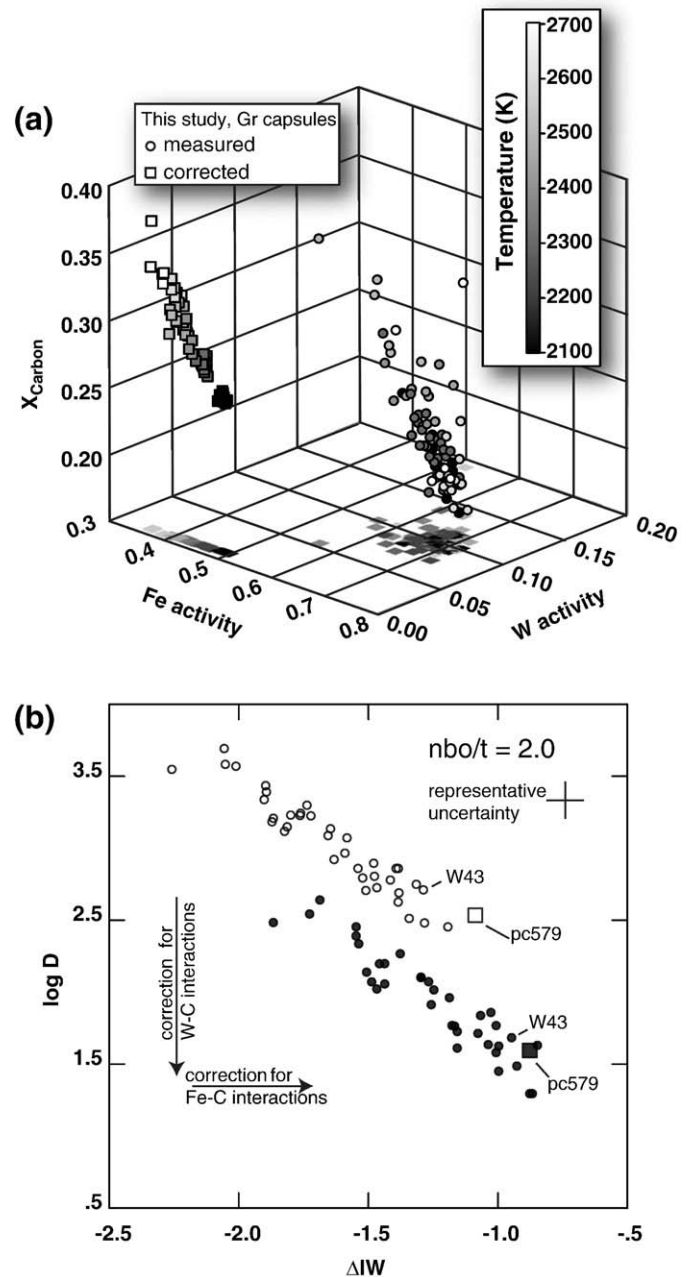


**Fig. 3.** W and Fe activity corrections due to the presence of carbon in liquid metal alloy. (a) Measured (mole fraction) and calculated (activities) of W, Fe, and C in the C-bearing experiments as a function of temperature for all experiments. Note that in this figure, correction for W–Fe activity in the metal has not been applied. Circles show the measured W, Fe, and C mole fractions (plotted as “activity,” assuming  $\gamma = 1$ ). Squares show the activities applied by METAL, described in detail in the text. These latter activities were used to calculate the molar partition coefficients and oxygen fugacities for the C-bearing experiments. (b) Effect of W–C and Fe–C activity corrections on the molar partition coefficient of W and on oxygen fugacity for 2 GPa experiments relative to the iron–wüstite (IW) buffer, normalized to a silicate melt composition with  $nbo/t = 2$ . Open circles = calculated “raw” molar partition coefficients and oxygen fugacity using the measured mole fractions of W and Fe in the metal phase. Shaded circles = corrected molar partition coefficients and oxygen fugacities after applying the activity corrections displayed in 3a. Carbon makes W and Fe more siderophile, therefore correction for carbon lowers partition coefficients and causes a shift to more oxidizing conditions relative to the IW buffer. Highlighted are carbon-bearing time-series experiments W43 and PC579 which are nearly duplicate experiments, but run in two different assemblies and analyzed separately on two different microprobes (see text for details). The metal analysis for experiment PC579 more faithfully captured the true metal composition (carbon content) and so there is less of a correction to  $a_{Fe}$ , and hence to the oxygen fugacity. The two experiments yield the same corrected molar partition coefficient and oxygen fugacity within the total error of our measurements (pressure, temperature, composition, and analysis).

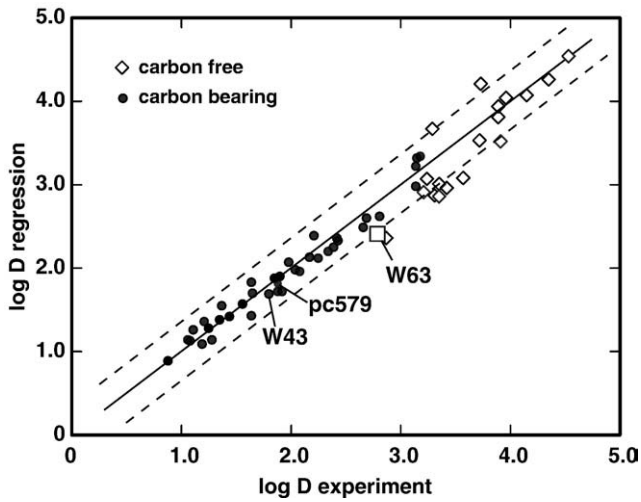


**Fig. 4.** Experiments performed at ~2 GPa (W63 in an MgO capsule) ( $n=57$ ). We compare the experimentally determined  $\log D$ , with metal activity corrections applied for W–C and Fe–C (METAL) and for W–Fe (O'Neill et al., 2008), to the  $\log D$  predicted by least-squares linear regression of the C-bearing experiments ( $n=37$ ) as a function of  $nbo/t$ ,  $\Delta IW$ , and  $1/T$ . C-free experiments ( $n=20$ ) are also plotted on this same figure without carbon activity corrections (but with W–Fe activity corrections).  $\log D$  of the C-free experiments are well-predicted by regression of the C-bearing experiments, indicating that the corrections applied to the C-bearing experiments are accurate. We note that the C-free solubility experiments (solid metal), the C-free partitioning experiments (liquid metal), and the corrected C-bearing experiments (liquid metal), can all be compared without further correction because solid metal/liquid metal partitioning of W is  $\sim 1$  (Chabot and Jones, 2003). Experiment pc579 was held at high pressure and temperature for 3 h, versus companion experiment W43, held for 10 min.

carbon-bearing systems, the free energy of dissolution at carbon saturation is constrained by the experimentally determined 1 atm melt + graphite liquidus as summarized by Shunk (1969).

For experiments in graphite capsules presented in this study, we input the temperature, and the Fe and W mole fractions (measured by electron microprobe), and C mole fraction (calculated “by difference” from the microprobe measurements). The program iteratively adjusted  $X_C$ , consistent with METAL’s model graphite saturation at the experimental  $T$ , and Fe and W fractions, and output the adjusted  $X_C$ ,  $a_{Fe}$ , and  $a_W$  (Wade and Wood, 2005). Fig. 3a compares measured Fe and W concentrations to calculated activities after accounting for interaction with carbon (where measured Fe and W activity are presented as if they were equal to their measured mole fractions in the metal, i.e. with  $\gamma=1$ ). Carbon causes an order of magnitude reduction in the activity of W to approximately 0.01 ( $\gamma_W \sim 0.1$ ), and reduces the activity of iron in the alloy to 0.4–0.5 ( $\gamma_{Fe} \sim 0.7$ ). These activity-composition relationships result in two important carbon-related shifts in the activity-corrected data: a shift to lower calculated partition coefficients and to higher calculated oxygen fugacities relative to the iron–wüstite buffer. The magnitude of these two shifts can be seen in Fig. 3b in which the measured partition coefficients and calculated partition coefficients, with activity corrections applied by METAL for W–C and Fe–C, for C-bearing experiments at 2 GPa are plotted.

METAL does not correct for Fe–W interactions (i.e. Wade and Wood (2005) assume that  $\gamma_{Fe} = 1$ ). METAL acts iteratively to adjust molar activities as described above, therefore W–Fe activity corrections cannot be applied to the experimental metals post facto; however, in order to compare our partition coefficients to W solubility experiments from the literature, and to apply our experimental results to a core-forming melt, we calculate the activity coefficient for W at infinite dilution in Fe ( $\gamma_W^{Fe,liq,\infty}$ ) metal according to Eq. (21) of O'Neill et al. (2008). The value of the activity coefficient varies from  $\sim 2$  to 8 across the temperature range of our experiments and is applied to both our C-bearing and C-free experiments as well as to solubility experiments from the literature. The results are reported in Table 1 as “ $\log D$  corrected.” These are the values plotted in Figs. 4–7.

### 3.4. Effect of oxygen fugacity and $nbo/t$ on partitioning

The oxygen fugacity relative to the iron–wüstite ( $\Delta IW$ ) equilibrium for experiments containing liquid Fe–alloy is:

$$\Delta IW = 2 \log \frac{a_{FeO}^{silicate}}{a_{Fe}^{metal}} \quad (2)$$

where  $a$  is the activity of FeO in the silicate and Fe in the metal (Hillgren et al., 1994). By assuming ideal solution behavior, we approximate the activity of FeO in silicate melt by the measured mole

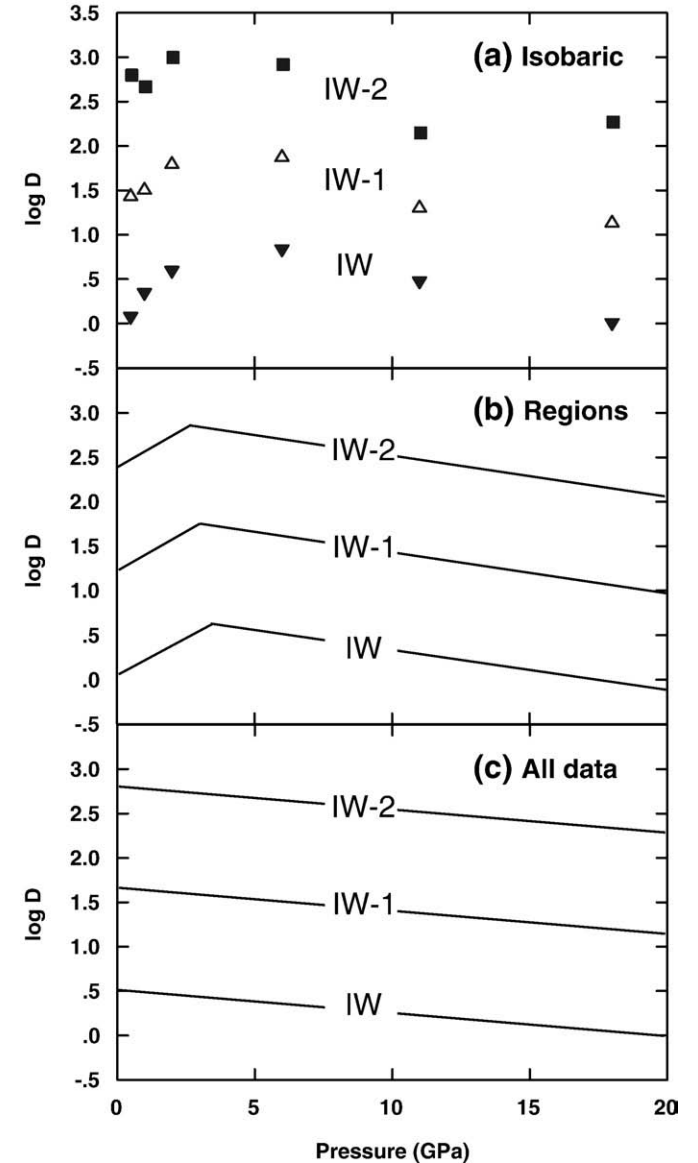


**Fig. 5.** Effect of pressure and oxygen fugacity on  $\log D$ , based on regressions to the data set given in Table 2 at three different oxygen fugacities IW–2, –1, and 0 and with data normalized to  $nbo/t=2.6$ . The data span a range of IW–0.8 to IW–1.5, so regressions at IW and IW–2 are extrapolations. Panel (a) plots isobaric data, and so is discretized for each pressure while panels (b–c) plot regressions across a range of pressures, and so are continuous functions. (a) Isobaric regression at each discrete experimental pressure, with each yielding its own  $fO_2$  dependence. At 0.5, 1, 2 and 6 GPa values are calculated at 2100 K. At 11 and 18 GPa values at 2400 and 2500 K respectively. (b) Two region regression (0.5–2 GPa and 6–18 GPa) fitting the data sets to an equation in four variables  $\Delta IW$ ,  $nbo/t$ ,  $1/T$  and  $P/T$  at 2500 K. The trends therefore interpolate between experimental pressures. (c) As in (b), but a global regression including data from all pressures (0.5 to 18 GPa,  $n=82$ ) with a resulting  $R^2$  of 0.92, a global valence of 4.6 ( $\pm 0.3$ ) and a mild negative pressure effect. The isobaric and regional regressions indicate that this global fit to the data is unwarranted.

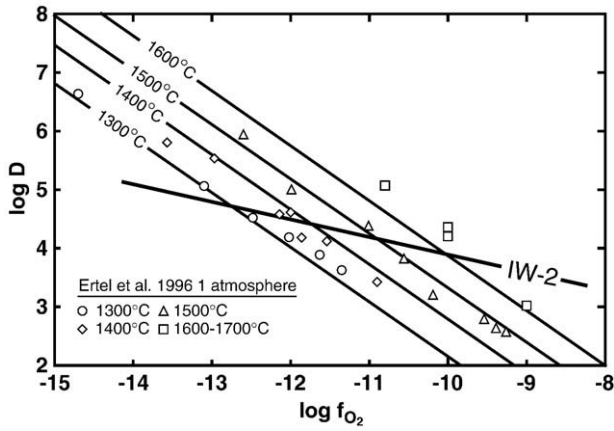


**Fig. 6.** Solubilities from Ertel et al. (1996), recalculated to infinite dilution in iron metal ( $\log D$ ) according to O'Neill et al. (2008), as a function of temperature and absolute oxygen fugacity. By calculating absolute  $f_{\text{O}_2}$  of the iron–wüstite buffer,  $-2$  log units, at  $1300^\circ\text{C}$  ( $-\log f_{\text{O}_2} = -12.75$ ) and  $1600^\circ\text{C}$  ( $-\log f_{\text{O}_2} = -9.97$ ), we plot the intersection of  $\Delta\text{IW} - 2$  with the experimental isotherms. We find that the slope is much shallower, such that, at constant absolute  $f_{\text{O}_2}$ , the partition coefficient strongly increases with temperature; however, along a constant buffer, the partition coefficient decreases with temperature. This result holds when the same analysis is applied to the measured solubilities (without conversion to partition coefficient). The effect of temperature on  $\log D$  seen in the Ertel data is consistent with, but slightly stronger than, what we observe, and opposite in sign to that applied by Wade and Wood (2005).

fraction,  $X_{\text{FeO}}$ . Although FeO is not likely to mix ideally in the silicate liquid, measured activity coefficients range from less than 1 to greater than 2 (e.g. Roeder, 1974; Holzheid et al., 1997), but it is not clear which activity coefficients would apply to the ultramafic liquids in our experiments. Where the activity of Fe in the metal has been corrected for Fe–C interactions by METAL, that activity is used in the denominator. The oxygen fugacities calculated using the measured or “raw” iron mole fractions range from about  $\text{IW} - 2.5$  to  $-1.5$ , with the C-corrected fugacities ranging from  $\text{IW} - 2$  to  $-0.75$  (Table 1 and Fig. 3). In our C-free experiments (with no additional solutes) we approximate the Fe activity by the mole fraction (i.e.  $X_{\text{Fe}}$ ).

We parameterize the degree of melt polymerization using the ratio of non-bridging oxygens to tetrahedrally coordinated oxygens ( $\text{nbo}/t = 0\text{--}4$ ) as defined by Mysen (1988, 1991). While  $\text{nbo}/t$  cannot capture pressure or temperature related changes in coordination or distinguish between CaO and MgO components in the silicate melt (O'Neill et al., 2008),  $\text{nbo}/t$  is the “industry standard” for collapsing the complex silicate melt compositions into a single term.

With these terms, we regressed sets of C-corrected partition coefficients using least squares multi-variable linear regression to an equation of the general form:

$$\log D = \alpha + \beta(\Delta\text{IW}) + \chi(\text{nbo}/t) + \delta(1/T) + \varepsilon(P/T) \quad (3)$$

Isobaric data sets reduce to three variables, and isobaric, isothermal data sets reduce to only two variables. Regression results are provided in Table 2.

The data set at 2 GPa is especially informative because it is the largest isobaric data set ( $n = 37$ ), as well as the pressure at which the C-free experiments ( $n = 19$ ) were performed. The least-squares best fit regression of the 2 GPa C-bearing experiments is compared to the experimentally determined values of  $\log D$  on Fig. 4. The C-free experiments have also been plotted, although they were not included in the regression. Eq. (3) accounts for 96% of the variance observed in the C-free data and 95% when the  $1/T$  term is excluded. This is a testament to the strong systematic control that oxygen fugacity and melt structure exert on W partitioning, confirming the affinity of W for more depolymerized melts (Walter and Thibault, 1995; Hillgren et al., 1996; Jana and Walker, 1997b) and more oxidized melts (Schmitt et al., 1989; Ertel et al., 1996; Jaeger and Drake, 2000).

The second salient feature of Fig. 4 is that almost all of the data from the carbon-free experiments that were not included in the regression fall within the 2 standard errors of the regression. Indeed, inclusion of the C-free experiments in the regression barely changes the regression coefficients ( $n = 57$ ,  $R^2 = 0.94$ ), even with the diversity of experimental methods and means of estimating the oxygen fugacity (Table 2).

The equilibrium between W metal and a dissolved W oxide component in the melt may be described by:



Eq. (4) predicts that there should be a linear relationship (as formulated in Eq. (3)) between oxygen fugacity ( $\log f_{\text{O}_2}$  or  $\Delta\text{IW}$ ) and  $\log D$  with a slope equal to  $x/4$ , where  $x$  is the valence state of

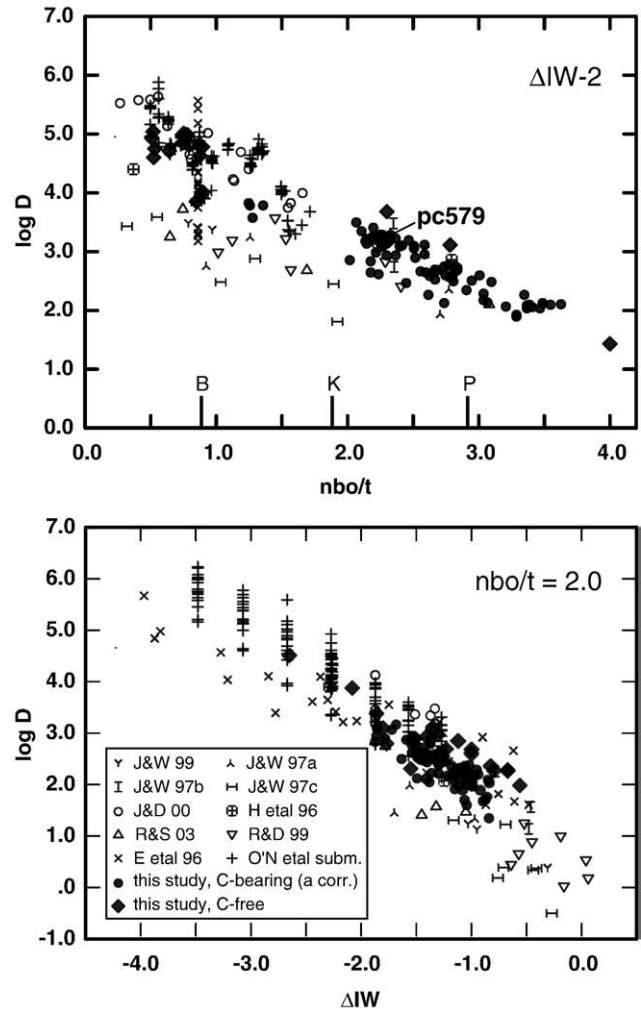


**Fig. 7.** Iron–alloy/silicate partitioning data for W as a function of melt composition and oxygen fugacity from the literature (Ertel et al., 1996; Hillgren et al., 1996; Jana and Walker, 1997a,b; 1997c, 1999; Righter and Drake, 1999; Righter and Shearer, 2003) and this study (with the exception of Schmitt et al., 1989 for which molar  $D$ s could not be reconstructed because an unknown amount of radioactive W tracer was added to the experiments., Palme, pers. comm.). We applied  $\gamma_{\text{W}}^{\text{FeO}}$  from O'Neill et al. (2008) as a function of temperature to convert solubility data from the literature to partition coefficients. Molar metal compositions for all experiments were activity corrected for solute interactions by METAL. (a)  $\log D(\text{W})$  as a function of  $\text{nbo}/t$ . All molar  $D$  values corrected to a common relative oxygen fugacity of  $\text{IW} - 2$  assuming a  $5+$  valence state for W. We show the representative values of  $\text{nbo}/t$  for basalt (B), komatiite (K) and peridotite (P). (b)  $\log D(\text{W})$  as a function of relative oxygen fugacity. All  $D$  values corrected to a common  $\text{nbo}/t$  of 2, assuming an  $\text{nbo}/t$  effect of  $-0.85$  log units per  $\text{nbo}/t$  unit as derived from regressions in Table 2.

**Table 2**

Results of multivariate linear regressions to corrected molar W partitioning data.

	<i>P</i> (GPa)	<i>T</i> (K)	<i>n</i>	$\alpha$	$\beta$ ( $\Delta IW$ )	$\chi$ (NBO/T)	$\delta$ (1/ <i>T</i> ); <i>p</i> -value †	$\epsilon$ ( <i>P</i> / <i>T</i> )	Standard Error	<i>R</i> <sup>2</sup>	valence
with W–Fe activity corrections applied	0.5	2100	5	3.48 (24)	–1.37 (17)	–1.31 (11)	–	–	0.07	0.97	5.5 (7)
	1	2100	12	2.40 (25)	–1.17 (13)	–0.79 (6)	–	–	0.11	0.97	4.7 (5)
	2	2300	15	2.66 (23)	–1.23 (13)	–0.85 (6)	–	–	0.12	0.96	4.9 (5)
	2	2450	8	2.52 (17)	–1.13 (9)	–0.83 (4)	–	–	0.07	0.99	4.5 (4)
	2	2600	14	2.36 (31)	–1.36 (17)	–0.83 (7)	–	–	0.12	0.97	5.4 (7)
	2	2300 – 2600	37	1.44 (40)	–1.21 (9)	–0.86 (4)	2894 (1010); 0.007	–	0.13	0.96	4.8 (4)
	2	1723 – 2673	57 ‡	1.92 (31)	–0.95 (10)	–0.90 (3)	2874 (774); 0.001	–	0.24	0.94	4.4 (4)
	6	2300	12	3.31 (20)	–1.01 (7)	–0.98 (5)	–	–	0.06	0.99	4.0 (3)
	6	2700	6	2.25 (1.1)	–1.24 (43)	–0.77 (26)	–	–	0.19	0.90	4.9 (1.7)
	6	2300 – 2700	18	1.77 (46)	–1.05 (12)	–0.92 (8)	3033 (841); 0.003	–	0.11	0.96	4.2 (5)
	11	2400	4	2.40 (35)	–0.85 (24)	–0.74 (7)	–	–	0.07	0.97	3.4 (9)
	18	2500	6	1.78 (40)	–1.13 (23)	–0.68 (12)	–	–	0.12	0.91	4.5 (9)
	0.5 – 2	2100 – 2600	54	1.72 (38)	–1.18 (7)	–0.85 (3)	1381 (755); 0.07	445 (127)	0.13	0.96	4.7 (3)
	6 – 18	2300 – 2700	28	1.66 (48)	–1.09 (11)	–0.85 (7)	3380 (1003); 0.003	–112 (13)	0.13	0.94	4.4 (4)
	0.5 – 18	2100 – 2700	82	2.74 (27)	–1.15 (8)	–0.85 (4)	–87 (610); 0.89	–63 (11)	0.17	0.92	4.6 (3)
without W–Fe activity corrections applied	2	1723 – 2673	57 ‡	2.19 (31)	–1.11 (7)	–0.89 (3)	524 (667); 0.44	–	0.2	0.95	4.4 (4)
	6	2300 – 2700	18	2.21 (46)	–1.05 (12)	–0.92 (8)	782 (841); 0.37	–	0.11	0.96	4.2 (5)
	6 – 18	2300 – 2700	28	2.10 (48)	–1.09 (11)	–0.85 (7)	1128 (1003); 0.27	–112 (13)	0.13	0.95	4.4 (4)
weight based regressions used in modeling	0.5 – 2	2100 – 2600	54	1.11 (39)	–1.18 (7)	–0.85 (3)	1680 (766); 0.03	487 (128)	0.14	0.95	4.7 (3)
	2	2300 – 2600	37	0.84 (41)	–1.22 (9)	–0.85 (4)	3245 (1026); 0.003	–	0.13	0.96	4.9 (4)
	6	2300 – 2700	18	1.17 (51)	–1.06 (13)	–0.90 (9)	3337 (942); 0.003	–	0.12	0.95	4.2 (5)
	6 – 18	2300 – 2700	28	1.05 (51)	–1.10 (11)	–0.84 (7)	3588 (1067); 0.003	–102 (14)	0.14	0.94	4.4 (4)

Uncertainty on regression coefficients is one standard error.

†*P*-values for all other coefficients are <0.0001.

‡Regression of all 2 GPa data, C-free and C-bearing (corrected).

W dissolved in the silicate melt. Thus, regression of the 2 GPa carbon-bearing data yields a regression coefficient for  $\Delta IW$  equal to  $-1.21 \pm 0.09$ , or a calculated valence of  $4.8 \pm 0.4$ , which is consistent with  $W^{+5}$ , or perhaps more likely a mixture of  $W^{+4}$  and  $W^{+6}$  (Table 2). New experimental data combined with X-ray Absorption Near Edge Structure (XANES) indicate that  $W^{+6}$  is the dominant species at 1 atm (O'Neill et al., 2008). Indeed, we calculate the same average valence (+5.5) for our lowest pressure experiments at 0.5 GPa as we do for the 1 atm data set from O'Neill et al. (2008) of +5.6. As our experimental pressures increase, however, the calculated average valence state tends to decrease toward  $W^{+4}$ , although the error in the calculated valence is large in the higher pressure data due to the low numbers of experiments and narrow range of  $fO_2$  coverage.

The regression of the 2 GPa data also shows a strong negative dependence on nbo/t, with a regression coefficient equal to  $-0.86 \pm 0.04$ , consistent with that reported by Walter and Thibault (1995). The ability of the silicate melt to accept W, a high valence network modifying cation, improves as more “free oxygen” becomes available to complex with W, either through increased oxygen content or depolymerization that increases overall oxygen availability (Hess, 1991).

### 3.5. Effect of temperature on partitioning

A potential exists to conflate the effects of pressure and temperature when parameterizing polybaric, polythermal, data sets if higher pressure experiments are also at higher temperatures. Our data set is well suited for assessing the temperature effect because we have a large number of isobaric experiments at both 2 and 6 GPa, and because in polybaric parameterizations the higher pressure experiments are not at progressively higher temperature.

Table 2 gives the regression coefficients for the term (1/*T*). Coefficients from regressions made both before the application of  $\gamma_{W}^{Fe,liq}$  from O'Neill et al. (2008), and after, are provided for data sets at 2 GPa and 6–18 GPa. We compare the results this way because there is a temperature effect imposed upon the data when correcting for Fe–W interactions. Before the Fe–W correction, the (1/*T*) coefficient for these regressions are positive (~500 to 1000), but the standard errors are large and the *P*-values on the (1/*T*)

coefficients are all >0.05. The 1/*T* coefficients are not statistically meaningful; there is no resolvable temperature effect. In contrast, after the Fe–W correction is applied to the data, the (1/*T*) coefficients remain positive but are about a factor of 3 to 5 larger (~3000), and have *P*-values less than 0.05. This difference is clearly a result of the temperature effect implicit in the Fe–W correction of O'Neill et al. (2008). The positive coefficient deduced here yields a mild negative effect of temperature on  $\log D(W)$  over the experimental pressure range.

### 3.6. Effect of pressure on partitioning

Fig. 5 shows  $\log D(W)$  as a function of pressure as calculated from the multivariate regressions. In this figure we hold the nbo/t term constant at a peridotitic value of 2.6, and show variation in  $\log D(W)$  at three different oxygen fugacities relative to the iron-wüstite buffer ( $\Delta IW = 0, -1$  and  $-2$ ). We note that the activity-corrected data set spans a range in relative  $fO_2$  of  $\sim IW - 0.8$  to  $IW - 1.5$  (average =  $IW - 1.2$ ), so that model *D*s outside this range are extrapolations.

Fig. 5a shows  $\log D(W)$  at each discrete pressure for which partitioning data were regressed in isolation against  $fO_2$ , nbo/t, and 1/*T*. At  $IW - 1$ ,  $\log D(W)$  shows an initial increase with pressure, then a decrease above ~3 to 4 GPa. Note, however, that at  $IW - 2$ ,  $\log D(W)$  shows no systematic pressure dependence. This arises because each isobaric regression yields its own  $fO_2$  dependence and model valence (Table 2). The uncertainties in the regressed  $fO_2$  parameters, which are especially large in regressions with few data (e.g. 0.5 and 11 GPa), do not justify the apparent  $fO_2$ -dependent pressure effect shown in Fig. 5a. Deducing the effect of pressure at  $\sim IW - 1$  is most appropriate, and a reversal in the pressure effect at ~3 to 4 GPa is strongly implicated. This change in slope in the pressure dependence might occur as a result of changes in silicate melt structure with pressure, such as the formation of more octahedrally coordinated silicons (Keppler and Rubie, 1993), or some other melt structural control, such as a change in W valence with pressure.

Relying on the trend observed at  $IW - 1$  in the isobaric regressions as a guide, we regressed the data set in two regions as a function of four variables (*P*, *T*,  $fO_2$  and nbo/t): all data from 0.5–2 GPa (*n* = 54)

and all data from 6 to 18 GPa ( $n = 28$ ). When the data are regressed in this way each pressure region has its own model  $fO_2$  dependence. The low- and high-pressure regression regions yield  $R^2$  values of 0.96 and 0.94 with calculated valence states of  $4.7 (\pm 0.3)$  and  $4.4 (\pm 0.4)$ , respectively. The regressions (Fig. 5b), which in contrast to panel (a), are continuous functions, reveal a strong increase in  $\log D(W)$  with pressure from 0.5 to 2 GPa and a moderate decrease with pressure from 6 to 18 GPa that is comparable in magnitude to that found for Ni (Thibault and Walter, 1995; Li and Agee, 1996, 2001). These trends are also seen in the uncorrected data and therefore are not likely to be an artifact of our activity corrections, which are necessarily based on studies at one atmosphere. The sharp inflection point is an artifact of the regression procedure, and is likely a continuous feature as speciation changes are controlled by homogeneous equilibria.

#### 4. Discussion I: comparison with previous studies

##### 4.1. Effect of carbon content, temperature, and pressure

As described in the previous section, regressions of the activity corrected data set predict a slight decrease in  $\log D(W)$  with increasing temperature at the experimental pressures. Yet  $W$  has been cited as one of a few elements that becomes more siderophile with increasing temperature (Ertel et al., 1996; Righter et al., 1997). We plot the results of Ertel et al. (1996) in Fig. 6 as a function of temperature and absolute  $fO_2$  at 1 bar. Also shown is  $fO_2$  plotted relative to the iron-wüstite buffer calculated from thermochemistry (O'Neill and Pownceby, 1993). The experiments of Ertel et al. (1996) demonstrate convincingly that  $\log D(W)$  increases strongly as a function of  $T$  at constant absolute  $fO_2$ , rising nearly 1.5 log units over a  $300^\circ$  rise in temperature. However, when considered in a buffer reference frame,  $\log D(W)$  decreases with temperature as shown on Fig. 6. Regression of the Ertel et al. (1996) data as a function of relative  $fO_2$  and temperature yields a  $(1/T)$  coefficient of  $\sim 8000$  ( $\sim 6000$  before application of  $\gamma_W^{Fe^{liq.\infty}}$ ). This temperature effect is the same in sign but about twice the magnitude we observe in our isobaric data sets and 2 and 6 GPa (Table 2). We also note, however, that the valence calculated from the  $fO_2$  dependence predicted by regression to the Ertel et al. (1996) data is  $\sim +3.8$ , inconsistent with the predicted value of  $\sim +5.5$  at 0.5 GPa from this study as well as the XANES results of O'Neill et al. (2008) at 1 bar ( $+5.6$ ).

The large and positive  $(1/T)$  term implied in the Ertel et al. data at 1 bar is in conflict with the negative coefficient ( $-1605$ ) applied to  $W$  by Wade and Wood (2005). The parameterization for  $W$  in the model by Wade and Wood (2005) is based on the data from 0.5 to 18 GPa presented here (corrected for C–W interactions by METAL, but uncorrected for  $W$  at infinite dilution in Fe metal,  $\gamma_W^{Fe^{liq.\infty}}$ ), but with some potentially important differences. In their study,  $W$  partitioning was expressed as an exchange coefficient,  $K_D$ , with a presumed valence of  $W^{4+}$ , which is not entirely justified by the data over the pressure range (Table 2). Wade and Wood regressed the  $K_D$  values as a function of the terms  $1/T$ ,  $P/T$  and  $nbo/t$  using data from 0.5 to 18 GPa, which has the effect of obfuscating the change in pressure effect we see at low pressures, and results in an opposite temperature effect. We discuss the implications of this study for the model of Wade and Wood (2005) later in the discussion.

Righter and coworkers (Righter et al., 1997; Righter and Drake, 1999; Righter and Shearer, 2003) attempted to isolate and parameterize the effects of intensive variables on  $D_{met/sil}$  for a suite of siderophile elements, including  $W$ , using multiple-linear regression. They deduced a range of temperature effects when all other variables were held constant. For example, at  $IW = 1$ , Righter et al. (1997) deduced a strong positive temperature effect on  $D_{met/sil}$  for  $W$ , whereas Righter and Shearer (2003) found a mild negative effect, consistent with our results. We postulate that the cause of their strong positive temperature dependence was likely carbon activity because the high temperature experiments were carbon-saturated and the low

temperature experiments were carbon-free. The regression of Righter et al. (1997) did not include  $X_C$  as a term, whereas Righter and Drake (1999) and Righter and Shearer (2003) did.

##### 4.2. Effect of pressure

In contrast to the negative pressure effect on  $D(W)$  observed by us at high pressures when relative  $fO_2$  is held constant, a positive effect was predicted in all the parameterizations of Righter and co-workers. The divergent result holds regardless of the form of the variables used in the regression (i.e. the sign and magnitude of the regression coefficient depends on the thermodynamic form ( $P$  vs  $P/T$ ) and whether absolute or relative  $fO_2$  are applied). Previous parameterizations were heavily biased by low-pressure data, which does in fact have a positive pressure effect, and must have suffered from the conflation of effects of pressure and carbon. Additional bias may have been introduced by the data of Ertel et al. (1996) which implicated  $W^{4+}$  rather than  $W^{+6}$  in solution. This reaffirms the caution required when extrapolating data to high pressures from a limited, low-pressure database.

A negative pressure effect for  $D(W)$  is unsurprising considering that other siderophile elements such as Ni, Co, Ga, and P are all known experimentally to become more lithophile with pressure at constant relative  $fO_2$  (Thibault and Walter, 1995; Li and Agee, 1996; Righter and Drake, 2000; Li and Agee, 2001; Kegler et al., 2008); however, as shown with temperature, it is critical also to evaluate the effect of pressure on the iron-wüstite buffer itself. For example, Campbell et al. (2007) have shown that as pressure increases the Ni:NiO and Fe:FeO buffers converge. Some of the experimentally observed behavior of  $D(Ni)$  with pressure can be attributed to this effect. High pressure data on the relative slopes of the Fe:FeO and  $W:WO_2$  buffers are not yet available, but 1 atmosphere thermoelastic data suggest divergence of the buffers with pressure, which should produce more siderophile  $W$  at high pressure relative to the iron-wüstite buffer. In that case, the negative pressure effect we observe would be less than the 'real' pressure effect, and can thus be considered a minimum dependence.

##### 4.3. Effect of oxygen fugacity, $W$ valence, and melt structure

The average  $W$  valence for our 0.5–2 GPa experiments is  $+5$ . Assuming  $W^{+5}$  and the  $nbo/t$  effect derived from our 2 GPa data set, we compare our experiments to all previously reported  $W$  partitioning experiments and solubility experiments in the metal-silicate system regardless of  $T$  or  $P$ , excluding only those experiments with metal compositions that deviated substantially from "Fe alloy" (e.g. Jana and Walker, 1999 with 88 wt.% Mo in the metal) and those for which molar partition coefficients could not be calculated (e.g. Schmitt et al., 1989). We applied METAL to all of the experiments (after calculating molar partition coefficients) to account for solute interactions over the range for which METAL is calibrated (e.g. solute interactions due to S less than 10 wt.%). We also applied  $\gamma_W^{Fe^{liq.\infty}}$  from O'Neill et al. (2008) to calculate  $\log D(W)$  at infinite dilution in Fe metal before normalizing to  $IW = 2$  with  $\beta = -1.21$  (Fig. 7a) and  $nbo/t = 2.0$  (Fig. 7b).

Our high pressure data show the same dependence on  $nbo/t$  and  $\Delta IW$  as the 1 atm data sets, indicating that neither pressure nor temperature account for a large measure of the variance relative to compositional terms. Experiments with additional solutes (e.g. Ni, Mo, Ga, P, S etc.) fall off of this trend, scattering to more lithophile values in both Fig. 7a and b. This is not an artifact of the corrections applied by METAL or  $\gamma_W^{Fe^{liq.\infty}}$ . Rather, because METAL does not account for multiple-solute (e.g. ternary) interactions at high abundance levels, multiple-dopant studies may contain unquantifiable solute-solute interactions. We conclude that solutes should therefore be studied in isolation when doping levels are very high, or, if investigating multiple solutes simultaneously, doping should remain at ppm levels (e.g. Chabot and Jones, 2003).

## 5. Discussion II: equilibrium core formation in Earth

Previous equilibrium models of core formation in Earth have shown that the partitioning behavior of an array of siderophile elements can apparently satisfy observed mantle abundances if metal and silicate equilibrated in a deep magma ocean. Here, we critically assess whether  $W$  is consistent with single-stage or multi-stage equilibrium core formation models. Fig. 8a shows the effect of pressure and  $f_{O_2}$  on the  $W$  partition coefficient, which we recalculate on a weight basis. We have fixed the  $nbo/t$  parameter to reflect complete melting of a peridotite magma ocean ( $nbo/t=2.6$ ). Oxygen fugacity contours are calculated with the assumption that metal/silicate equilibration is constrained to lie on the peridotite liquidus, using melting data from Tronnes and Frost (2002) and Zerr et al. (1998). The plot is based on the regression regions 0.5–2 GPa and 6–18 GPa (Table 2), which is our preferred model for the effect of pressure on  $D(W)$ . The value of  $\log D(W)$  needed for bulk equilibration of Earth's core and mantle is shown as a gray band ( $\log D(W)_{Earth}$ ), the width of which reflects the uncertainty in this value (Walter et al., 2000). When  $W$  is considered in isolation, the single-stage equilibrium model yields solutions that span the entire range of pressures considered (1 atm to 70 GPa). This wide range of permissible solutions occurs because the effects of pressure and  $f_{O_2}$  trade off. That is, for a low-pressure solution the system must be more oxidizing (e.g.  $\sim IW-1.5$  at 1 atm.), whereas higher-pressure solutions require more reducing conditions (e.g.  $\sim IW-3.0$  at 70 GPa.). Based on our knowledge of mantle FeO from xenoliths and seismology, it is likely that the bulk mantle has between 6 and 10 wt.% FeO, which yields a range in bulk Earth ( $f_{O_2}$ ) of  $\sim IW-2$  to  $IW-2.5$  (black band, Fig. 8). The intersection of the  $\log D(W)_{Earth}$  band and the Earth ( $f_{O_2}$ ) band describes the range of preferred solutions for this  $f_{O_2}$ -prescribed equilibrium model. The range of possible pressure solutions in the prescribed  $f_{O_2}$  range is about 20 to 50 GPa. Uncertainty is plotted on Fig. 8 as  $\pm 0.3$  log units, which is twice the standard error in  $\log D$  (Table 2, 6–18 GPa). Though we acknowledge that the range of preferred solutions lies outside of our experimental range, the present data set suggests that  $W$  in Earth's mantle is consistent with single-stage equilibration at high pressures, along the liquidus, in a shallow to moderately deep peridotite magma ocean.

Also plotted on Fig. 8 are appropriate representations of the pressure and  $f_{O_2}$  conditions predicted in a number of other single-stage siderophile-element based models, including those that considered Ni and Co in isolation (Li and Agee, 2001; Walter and Tronnes, 2004), and those that considered other elements as well (Richter and Drake, 1999; Gessmann and Rubie, 2000; Wade and Wood, 2005). In order for the  $P$ - $f_{O_2}$  conditions predicted by the previous models to be considered consistent with our modeled partitioning behavior of  $W$ , they should lie within the field labeled “preferred solution.”

At the conditions suggested by Richter and Drake (1999) of 27 GPa, our  $W$  results require that the  $f_{O_2}$  conditions be about 1 log unit more reducing than they propose. The more oxidizing conditions of Richter and Drake (1999) likely result from erroneous pressure and temperature effects in their calibration for  $W$ , as discussed in the previous section. The pressures deduced for core/mantle equilibration in other recent models are generally in the range of 40 to 50 GPa, and these just intersect or plot slightly below the  $\log D(W)_{Earth}$  band. This difference is accommodated by the uncertainty in the  $f_{O_2}$  contours associated with the regression. Thus, our  $W$  partitioning data is broadly consistent with multi-element single-stage core formation models.

If carbon makes up a component of the core, the picture changes. Carbon comprises 0.1 (McDonough, 2003) to 3.5 wt.% (Anders and Grevesse, 1989; Palme and Jones, 2003) of the bulk Earth, depending on how much carbon was lost during accretion. Considering solubility limits, this corresponds to 0.2–6 wt.% carbon in the core (Dasgupta and Walker, 2008). Such abundances would shift the  $f_{O_2}$  contours up

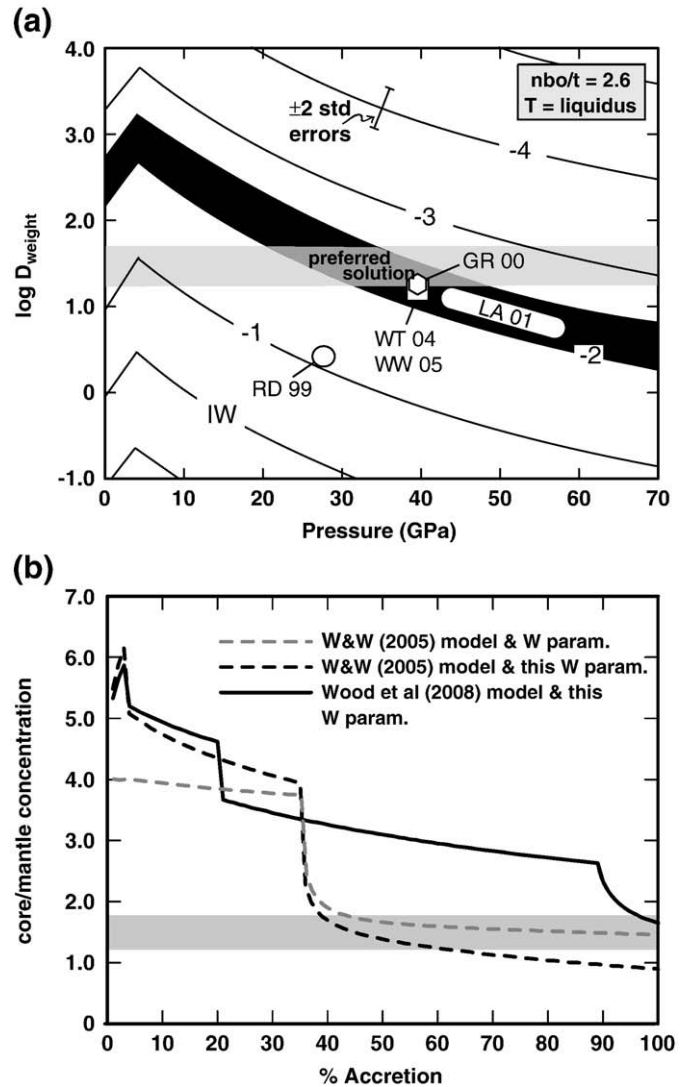


**Fig. 8.** (a) The effect of pressure and  $f_{O_2}$  on  $\log D(W)$  (weight-based) at  $nbo/t=2.6$ . Relative  $f_{O_2}$  ( $\Delta IW$ ) contours are calculated for temperature along a model peridotite liquidus and do not take into account the effect of composition on the liquidus. Representative regression uncertainty is shown on the  $\Delta IW-4$  contour. The horizontal gray band indicates the range of  $\log D(W)$  that would satisfy the mantle  $W$  abundance (Walter et al., 2000), and the black band shows the range of  $f_{O_2}$  consistent with the modern mantle FeO content ( $\Delta IW = -2$  to  $-2.5$ ). The region of intersection of the two bands in dark grey, labeled ‘preferred solution’, shows the range in pressures that satisfy the single-stage equilibrium model for carbon-free core formation in Earth examining  $W$  in isolation. Symbols indicate the model equilibrium core formation conditions predicted by previous workers (GR00 = Gessmann and Rubie, 2000; WT04 = Walter and Tronnes, 2004; WW05 = Wade and Wood, 2005; RD99 = Richter and Drake, 1999; LA01 = Li and Agee, 2001). The oxygen fugacity reported by Richter and Drake (1999) of  $IW-0.4$  uses Fe and FeO activities to arrive at a final equilibration  $f_{O_2}$ . That value was recalculated to  $IW-1.1$  to be consistent with the approach taken in the other studies plotted, including this one (i.e. taking the ratio of Fe to FeO); however, it may not be strictly equivalent, as Richter and Drake (1999) calculate absolute  $f_{O_2}$  at high PT. (b) Models of continuous, multi-stage core segregation during accretion with progressive oxidation. Two cases are shown that emulate models presented in Wade and Wood (2005) and Wood et al. (2008). Accretion is modeled in 1% Earth mass increments. The model of Wade and Wood (2005) is depicted by dashed lines on Fig. 8. The core segregates at the base of a magma ocean which is 46% of the depth to the core–mantle boundary. The pressure at the core–mantle boundary increases during accretion and the temperature path is fixed on the peridotite liquidus. There is an oxygen fugacity jump corresponding to an instantaneous change from 0.6% to 6.36% Fe in the mantle after 35% accretion. The grey dashed line shows this model using the  $W$  parameterization of Wade and Wood (2005). The black dashed line shows the same model using the polybaric parameterizations from this study (Table 2). The solid line shows a model as described in Fig. 7 of Wood et al. (2008). In this model the base of the magma ocean is fixed at 35% of the depth to the core–mantle boundary, and the oxidized Fe content of the mantle increases from 0.6% to 6.26% in two steps, at mass fractions of 0.2 (0.6 to 1.6% Fe) and 0.89 (1.6 to 6.26% Fe), during Earth accretion.

in Fig. 8 by 0.026 to 0.7 log units, which is the difference in  $\log D$  in C-free vs C-bearing systems (Fig. 3). This would shift the area of intersection of the gray W depletion band and the black  $fO_2$  band. A carbon-bearing core would be consistent with W partitioning at pressures ranging from  $\sim 30$  to greater than 70 GPa. The constraints on the  $P$ – $T$ – $fO_2$  of a model magma ocean therefore loosen considerably if the core contains a significant, but not unreasonable, amount of carbon.

An alternative scenario to single-stage equilibrium core formation is continuous accretion involving progressive oxidation during core formation (O'Neill, 1991) which has recently been popularized in the model of Wade and Wood (2005) and Wood et al. (2006, 2008). In their models, Wade and Wood (2005) and Wood et al. (2008) use both moderately siderophile (Ni, Co,  $\pm W$ ) and slightly siderophile (e.g. Si, V, Nb) elements to constrain pressure–temperature– $fO_2$  trajectories that can reproduce mantle abundances during continuous accretion with progressive oxidation. Given the differences between their parameterization of W partitioning (discussed above) and the present parameterization, and because W is sensitive to both pressure and  $fO_2$ , it is instructive to see whether our new parameterizations yield solutions consistent with those presented in the earlier models.

Fig. 8b shows the predicted core/mantle W ratio in two continuous accretion models based directly on the model parameters given in Wade and Wood (2005; Fig. 8) and Wood et al. (2008; Fig. 7). As a test to insure that our modeling is comparable, we successfully reproduced the Wade and Wood (2005) model using their parameterization for W (Fig. 8b). Using our new parameterizations, we find that the final core/mantle ratio predicted for the Wade and Wood (2005) model is no longer compatible with the observed mantle W abundance, being lower about 0.8 log units, although when all model uncertainties are considered the solution may be acceptable. In contrast, the model presented in Wood et al. (2008), which did not include W, yields a nominally acceptable fit for W based on our parameterization. Thus, we find that W is generally compatible with the continuous accretion and progressive oxidation models as presented in these previous studies.

## 6. Conclusion

Our experimental data set for W constrains the effects of a wide range of physical parameters on partitioning between liquid–metal and liquid–silicate. We find that W partitioning is highly sensitive to compositional parameters including oxygen fugacity, the silicate melt composition, and the metal carbon content. Much of this compositional sensitivity reflects the highly-charged nature of the W cation in silicate solution, with our data indicating a mixture of 6+ and 4+ oxidation states. We find that while pressure has a minor effect relative to compositional terms, it influences W partitioning to about the same extent that it influences Ni partitioning. In contrast to previous predictions, W partitioning is found to be relatively insensitive to temperature, with  $D(W)$  decreasing slightly as temperature increases. Elucidating the effects of temperature and pressure required isolation of the carbon effect and illustrates the need for cautious interpretation of experimental studies employing multiple solutes.

The observed variations in  $D(W)$  with experimental parameters are reproduced well by multi-variate regressions to the data, and we use these regressions to predict W partitioning over a wide range of conditions. We find that the W abundance in the modern mantle can be achieved in single-stage equilibrium models of core segregation along the liquidus in a peridotite magma ocean over a wide range of pressures and  $fO_2$ s, and this is due to a trade-off between these two parameters. However, when we prescribe the  $fO_2$  conditions to model values for mantle FeO contents (IW–2 to IW–2.5), the pressure range of acceptable solutions is limited to  $\sim 20$  to 50 GPa, or 30 to 70 GPa if carbon is a significant light element in the core. Continuous, multi-stage models for equilibrium core formation that invoke

progressive oxidation of the mantle as developed by Wade and Wood (2005) and Wood et al. (2008) remain viable given our new W data treatment.

## Acknowledgements

The authors thank Hugh O'Neill for sharing data in press, Amelia Logan for assistance with the electron microprobe, Yves Thibault for help with experiments, and Bernard Wood for supplying us with the code for program METAL. The manuscript benefited from reviews by Kevin Righter, Bernard Wood, Herbert Palme, and Nancy Chabot. This work was supported by the Smithsonian Institution, NSF, and NERC.

## Appendix A. Supplementary data

Supplementary data associated with this article can be found, in the online version, at doi:10.1016/j.epsl.2009.02.024.

## References

- Anders, E., Grevesse, N., 1989. Abundances of the elements: meteoritic and solar. *Geochim. Cosmochim. Acta* 53, 197–214.
- Benz, W., Cameron, A.G.W., 1990. In: Newsom, H.E., Jones, J. (Eds.), *Terrestrial Effects of the Giant Impact. Origin of the Earth*. Oxford Press, New York, pp. 61–68.
- Campbell, A.J., Danielson, L., Righter, K., Seagle, C.T., Wang, Y., Prakash, V.B., 2007. Oxygen fugacity buffers at conditions of the deep Earth. *EOS, Trans.-Am. Geophys. Union* 88 (52) Fall Meeting Suppl., Abstract MR23D-08.
- Canup, R.M., Righter, K., 2000. *Origin of the Earth and Moon*. University of Arizona Press.
- Chabot, N.L., Jones, J.H., 2003. The parameterization of solid metal–liquid metal partitioning of siderophile elements. *Meteorit. Planet. Sci.* 38 (10), 1425–1436.
- Chabot, N.L., Draper, D.S., Agee, C.B., 2005. Conditions of core formation in the earth: constraints from nickel and cobalt partitioning. *Geochim. Cosmochim. Acta* 69 (8), 2141–2151.
- Chabot, N.L., Campbell, A.J., Jones, J.H., Humayun, M., Lauer, J.H.V., 2006. The influence of carbon on trace element partitioning behavior. *Geochim. Cosmochim. Acta* 70 (5), 1322–1335.
- Chambers, J.E., 2004. Planetary accretion in the inner solar system. *Earth Planet. Sci. Lett.* 223 (3–4), 241–252.
- Cottrell, E. (2004). *Differentiation of the Earth from the Bottom Up: Core, Lithosphere, and Crust*. Department of Earth and Environmental Sciences, New York, Columbia University. Ph.D.: 163.
- Cottrell, E., Walker, D., 2006. Constraints on core formation from Pt partitioning in mafic silicate liquids at high temperatures. *Geochim. Cosmochim. Acta* 70 (6), 1565–1580.
- Dasgupta, R., Walker, D., 2008. Carbon solubility in core melts in a shallow magma ocean environment and distribution of carbon between the Earth's core and the mantle. *Geochim. Cosmochim. Acta* 72 (18), 4627–4641.
- Davies, G.F., 1985. Heat deposition and retention in a solid planet growing by impacts. *Icarus* 63 (1), 45–68.
- Ertel, W., O'Neill, H.S.C., Dingwell, D.B., Spettel, B., 1996. Solubility of tungsten in a haplobasaltic melt as a function of temperature and oxygen fugacity. *Geochim. Cosmochim. Acta* 60 (7), 1171–1180.
- Gessmann, C.K., Rubie, D.C., 2000. The origin of the depletions of V, Cr and Mn in the mantles of the Earth and Moon. *Earth Planet. Sci. Lett.* 184 (1), 95–107.
- Ghosh, A., McSween, H.Y., 1998. A thermal model for the differentiation of asteroid 4 Vesta, based on radiogenic heating. *Icarus* 134, 187–206.
- Gustafson, P., 1987. Thermodynamic evaluation of the C–Fe–W system. *Metall. Trans.* 18, 175–188.
- Hess, P.C. (Ed.), 1991. *The role of high field strength cations in silicate melts*. Physical Chemistry of Magmas. New York, Springer-Verlag.
- Hillgren, V.J., Drake, M.J., Rubie, D.C., 1994. High-pressure and high-temperature experiments on core–mantle segregation in the accreting Earth. *Science* 264 (5164), 1442–1445.
- Hillgren, V.J., Drake, M.J., Rubie, D.C., 1996. High pressure and high temperature metal–silicate partitioning of siderophile elements: the importance of silicate liquid composition. *Geochim. Cosmochim. Acta* 60 (12), 2257–2263.
- Holzheid, A., Palme, H., Chakraborty, S., 1997. The activities of NiO, CoO and FeO in silicate melts. *Chemical Geology* 139 (1–4), 21–38.
- J.S.f.P.o.S.a.T.T.Co. *Steelmaking*. Steelmaking Data Sourcebook, 1988. Montreux. Gordon and Breach Science Publishers.
- Jaeger, W.L., Drake, M.J., 2000. Metal–silicate partitioning of Co, Ga, and W: dependence on silicate melt composition. *Geochim. Cosmochim. Acta* 64 (22), 3887–3895.
- Jana, D., Walker, D., 1997a. The impact of carbon on element distribution during core formation. *Geochim. Cosmochim. Acta* 61 (13), 2759–2763.
- Jana, D., Walker, D., 1997b. The influence of silicate melt composition on distribution of siderophile elements among metal and silicate liquids. *Earth Planet. Sci. Lett.* 150 (3–4), 463–472.
- Jana, D., Walker, D., 1997c. The influence of sulfur on partitioning of siderophile elements. *Geochim. Cosmochim. Acta* 61 (24), 5255–5277.
- Jana, D., Walker, D., 1999. Core formation in the presence of various C–H–O volatile species. *Geochim. Cosmochim. Acta* 63 (15), 2299–2310.

- Kegler, P., Holzheid, A., Frost, D.J., Rubie, D.C., Dohmen, R., Palme, H., 2008. New Ni and Co metal–silicate partitioning data and their relevance for an early terrestrial magma ocean. *Earth Planet. Sci. Lett.* 268 (1–2), 28–40.
- Kepler, H., Rubie, D.C., 1993. Pressure-induced coordination changes of transition-metal ions in silicate melts. *Nature* 364 (6432), 54–56.
- Li, J., Agee, C.B., 1996. Geochemistry of mantle–core differentiation at high pressure. *Nature* 381 (6584), 686–689.
- Li, J., Agee, C.B., 2001. The effect of pressure, temperature, oxygen fugacity and composition on partitioning of nickel and cobalt between liquid Fe–Ni–S alloy and liquid silicate: implications for the Earth's core formation. *Geochim. Cosmochim. Acta* 65 (11), 1821–1832.
- Ma, Z.T., 2001. Thermodynamic description for concentrated metallic solutions using interaction parameters. *Metall. Mater. Trans., B, Proc. Metall. Mater. Proc. Sci.* 32, 87–103.
- McDonough, W.F., 2003. Compositional model for the Earth's core. In: Carlson, R.W. (Ed.), *The Mantle and Core, Treatise on Geochemistry*. Elsevier–Pergamon, Oxford, pp. 547–568.
- Mills, K., 1993. The influence of structure on the physico–chemical properties of slags. *ISIJ Int.* 33, 148–155.
- Mysen, B.O., 1988. *Structure and Properties of Silicate Melts*. Elsevier, Amsterdam.
- Mysen, B.O., 1991. Properties of magmatic liquids. In: Perchuck, L.L., Kushiro, I. (Eds.), *Physical Chemistry of Magmas*. Springer–Verlag, New York, pp. 70–75.
- O'Neill, H.S., 1991. The origin of the Moon and the early history of the Earth – a chemical–Model.2. *The Earth. Geochim. Cosmochim. Acta* 55 (4), 1159–1172.
- O'Neill, H.S., Pownceby, M.I., 1993. Thermodynamic data from redox reactions at high-temperatures.1. An experimental and theoretical assessment of the electrochemical method using stabilized zirconia electrolytes, with revised values for the Fe–FeO, Co–CoO, Ni–NiO and Cu–Cu<sub>2</sub>O oxygen buffers, and new data for the W–WO<sub>2</sub> buffer. *Contrib. Mineral. Petrol.* 114 (3), 296–314.
- O'Neill, H.S.C., Berry, A.J., Eggins, S.M., 2008. The solubility and oxidation state of tungsten in silicate melts: implications for the comparative chemistry of W and Mo in planetary differentiation processes. *Chem. Geol.* 255 (3–4), 346–359.
- Palme, H., Jones, J., 2003. Solar system abundances of the elements. In: Davis, A.M. (Ed.), *Meteorites, Comets, and Planets, Treatise on Geochemistry*. Elsevier Ltd, Amsterdam, pp. 41–61.
- Righter, K., Drake, M.J., 1999. Effect of water on metal–silicate partitioning of siderophile elements: a high pressure and temperature terrestrial magma ocean and core formation. *Earth Planet. Sci. Lett.* 171 (3), 383–399.
- Righter, K., Drake, M.J., 2000. Metal/silicate equilibrium in the early Earth – New constraints from the volatile moderately siderophile elements Ga, Cu, P, and Sn. *Geochim. Cosmochim. Acta* 64 (20), 3581–3597.
- Righter, K., Shearer, C.K., 2003. Magmatic fractionation of Hf and W: constraints on the timing of core formation and differentiation in the Moon and Mars. *Geochim. Cosmochim. Acta* 67 (13), 2497–2507.
- Righter, K., Drake, M.J., Yaxley, G., 1997. Prediction of siderophile element metal–silicate partition coefficients to 20 GPa and 2800°C: the effects of pressure, temperature, oxygen fugacity, and silicate and metallic melt compositions. *Phys. Earth Planet. Inter.* 100 (1–4), 115–134.
- Roeder, P.L., 1974. Activity of iron and olivine solubility in basaltic liquids. *Earth Planet. Sci. Lett.* 23 (3), 397–410.
- Sasaki, S., Nakazawa, K., 1986. Metal–silicate fractionation in the growing Earth – Energy–source for the terrestrial magma ocean. *J. Geophys. Res.–Solid Earth Planets* 91 (B9), 9231–9238.
- Schmitt, W., Palme, H., Wanke, H., 1989. Experimental–determination of metal silicate partition – Coefficients for P, Co, Ni, Cu, Ga, Ge, Mo, and W and some implications for the early evolution of the Earth. *Geochim. Cosmochim. Acta* 53 (1), 173–185.
- Shunk, F. A. (1969). New York, NY, McGraw–Hill.
- Thibault, Y., Walter, M.J., 1995. The influence of pressure and temperature on the metal–silicate partition–coefficients of nickel and cobalt in a model–c1 chondrite and implications for metal segregation in a deep magma ocean. *Geochim. Cosmochim. Acta* 59 (5), 991–1002.
- Tonks, W.B., Melosh, H.J., 1993. Magma ocean formation due to giant impacts. *J. Geophys. Res.–Planets* 98 (E3), 5319–5333.
- Tronnes, R.G., Frost, D.J., 2002. Peridotite melting and mineral–melt partitioning of major and minor elements at 22–24.5 GPa. *Earth Planet. Sci. Lett.* 197 (1–2), 117–131.
- Uhrenius, B., 1980. Calculation of phase equilibria in the Fe–W–C system. *Calphad* 4 (3), 173–191.
- Wade, J., Wood, B.J., 2005. Core formation and the oxidation state of the Earth. *Earth Planet. Sci. Lett.* 236 (1–2), 78–95.
- Walter, M.J., Thibault, Y., 1995. Partitioning of tungsten and molybdenum between metallic liquid and silicate melt. *Science* 270 (5239), 1186–1189.
- Walter, M.J., Tronnes, R.G., 2004. Early Earth differentiation. *Earth Planet. Sci. Lett.* 225 (3–4), 253–269.
- Walter, M.J., Newsom, H.E., Ertel, W., Holzheid, A., 2000. Siderophile elements in the Earth and Moon: Metal/silicate partitioning and implications for core formation. In: Canup, R.M., Righter, K. (Eds.), *Origin of the Earth and Moon*. University of Arizona Press, pp. 265–290.
- Walter, M.J., Thibault, Y., Wei, K., Luth, R.W., 1995. Characterizing experimental pressure and temperature conditions in multi–anvil apparatus. *Can. J. Phys.* 73 (5–6), 273–286.
- Wood, B.J., Walter, M.J., Wade, J., 2006. Accretion of the Earth and segregation of its core. *Nature* 441 (7095), 825–833.
- Wood, B.J., Wade, J., Kilburn, M.R., 2008. Core formation and the oxidation state of the Earth: Additional constraints from Nb, V and Cr partitioning. *Geochim. Cosmochim. Acta* 72 (5), 1415–1426.
- Yin, Q.Z., Jacobsen, S.B., Yamashita, K., Blichert–Toft, J., Telouk, P., Albareda, F., 2002. A short timescale for terrestrial planet formation from Hf–W chronometry of meteorites. *Nature* 418 (6901), 949–952.
- Yoshino, T., Walter, M.J., Katsura, T., 2003. Core formation in planetesimals triggered by permeable flow. *Nature* 422, 154–157.
- Zerr, A., Diegeler, A., Boehler, R., 1998. Solidus of Earth's deep mantle. *Science* 281 (5374), 243–246.